Materials Today Communications 39 (2024) 108790

Contents lists available at ScienceDirect

Materials Today Communications

journal homepage: www.elsevier.com/locate/mtcomm

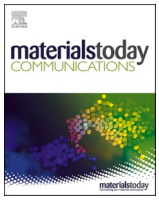

A data-driven rate and temperature dependent constitutive model of the compression response of a syntactic foam

Burcu Tasdemir [a], Vito L. Tagarielli [b,*], Antonio Pellegrino [c,*]

[a] School of Electrical, Electronic and Mechanical Engineering, University of Bristol, Bristol, UK
[b] Department of Aeronautics, Imperial College London, London, UK
[c] Department of Mechanical Engineering, University of Bath, Bath, UK

ARTICLE INFO

Keywords:
Foams
Impact behaviour
Statistical properties/methods
Mechanical testing
Machine learning

ABSTRACT

Polymeric syntactic foams are used in aerospace and marine applications requiring low density and low moisture absorption together with high specific strength and stiffness. Their mechanical response is highly sensitive to temperature and strain rate and such sensitivity must be modelled accurately. In this study, the uniaxial compressive response of a polymeric syntactic foam is measured at strain rates in the range $[10^{-3}, 2.5{\cdot}10^{3}]$ /s and temperatures varying between −25°C and 100°C. The resulting dataset is used to train a neural network to predict the compressive response of the foam at arbitrary strain rates and temperatures. It is found that the surrogate model is highly effective in predicting the material response at temperature and rates not included in its training set. Finally, a stochastic version of the data-driven model to allow predictions of the variability in the stress versus strain response is proposed.

1. Introduction

Polymer syntactic foams are a composite of polymer and glass microspheres. The inclusion of hollow glass micro-balloons enhances their mechanical properties and specific energy absorption while reducing the moisture intake due to their closed-cell moisture-impermeable structure [1]. These attributes make this class of materials well suited for applications in the submarine, automotive, and aerospace industry. The mechanical behaviour of these reinforced foams depends strongly on the rate of deformation and the temperature, owing to the inherent strain rate and temperature dependency of the polymer matrix as well as the energy-dissipating nature of deformation and breakage of the microspheres [2–4].

Numerous research efforts have investigated the dynamic response of syntactic foams under ambient conditions [5–9]. However, syntactic foams are used in a diverse environmental settings, including extreme temperatures, owing to their thermal insulation properties [10,11]. The effect of temperature on the compressive response and failure mechanisms of zinc syntactic foams with different particle fillers were investigated in [12]. The rate dependent compressive response of Aluminium syntactic foams with matrices of different composition and heat treatment was studied in [13]. More recently, Movahedi et al. [14] examined the response of functionally graded aluminium syntactic foams under compressive impact loading.

Given the temperature-dependent nature of the polymer matrix [15], the physical and mechanical properties of polymer syntactic foams exhibit considerable sensitivity to variations in temperature [16]. Tan et al. [17] explored the temperature and strain rate dependence of an epoxy syntactic foam under tensile and shear load. The interplay between the influence of strain rate and temperature on the compressive and tensile response of three different polymer syntactic foams was analysed in [18].

In this study, supervised machine learning is employed to model the behaviour of an epoxy syntactic foam under compression, considering variations in strain rate and temperature. Machine learning has found numerous applications in the field of solid mechanics with the purpose to accelerate or enable complex material design and optimisation. These applications include, among the others, the development of constitutive models for metallic materials [19,20], reverse engineering [21], structure generation [22] of additively manufactured materials as well as modelling and design of composite materials [23]. However, the existing literature does not include any application of machine learning aiming at predicting the mechanical characteristics of syntactic foams considering their dependence on temperature and strain rate.

* Corresponding authors.
E-mail addresses: v.tagarielli@imperial.ac.uk (V.L. Tagarielli), ap3551@bath.ac.uk (A. Pellegrino).

https://doi.org/10.1016/j.mtcomm.2024.108790
Received 21 January 2024; Received in revised form 12 March 2024; Accepted 29 March 2024
Available online 1 April 2024

This study focuses on an epoxy-based syntactic foam and presents measurements of its uniaxial compressive response at strain rates and temperatures in the ranges [10^{-3}, $2.5{\cdot}10^{3}$] /s and [-25, 100] °C, respectively. The measurements are used to train a surrogate able to predict the mechanical response of the material at arbitrary temperature and strain rate within the testing ranges. A second model that can also predict the uncertainty in the compressive response at arbitrary rate and temperature is then implemented. A flowchart illustrating the general process employed in this study is illustrated in Fig. 1. The proposed technique can be applied to any solid material; however, a syntactic foam is chosen for this study due to its wide availability, extensive industrial usage, and significant dependence on temperature and strain rate.

The paper is structured as follows. Section 2 outlines the studied material and experimental methods; Section 3 presents the measured results, the data-driven surrogate models and discusses their accuracy.

2. Material and methods

2.1. Material and specimens

The material investigated is an epoxy-based syntactic foam, made of glass microspheres of diameter from 15 to 60 μm, a mean wall thickness of 0.8 μm, and a volume fraction of 0.5. The employed glass microballoons were made of soda-lime borosilicate glass, surface treated for enhanced coupling with epoxy resins. The investigated syntactic foam is a structural 2-part void filling compound commercialised under the name of EC-3524 B/A produced by 3 M Scotch Weld. The two parts were weighted and mixed manually for approximately 15 seconds after a uniform colour was obtained. The mixture was slowly stirred until a uniform compound was obtained. The compound was cast in stainless steel moulds to obtain syntactic foam slabs. The slabs were then cured for 48 hours at room temperature. The foam was produced and provided by an external company and received in the form of cylinders od diameter 22.5 mm and length 150 mm. The overall material density was measured as 500 kg/m^3.

The microstructure of the foam was visualized by observing portion of unstable fracture surfaces, as shown in the micrograph of Fig. 2. Microbubbles of varying sizes are visible, of size distribution consistent with that reported in the manufacturer's datasheet.

Circular cylindrical samples, measuring 5 mm in diameter and 2.5 mm in height, were employed in high-rate and quasi-static compression experiments. This choice was informed by prior research, which suggested that the ideal aspect ratio (height to diameter ratio) for compression specimens falls within the range of 0.5–1 [24]. The lower bound of this range is adopted to favour of the attainment of force equilibrium and to increase the achievable strain rates.

The specimens were speckled to enable for the Digital Image Correlation (DIC) analysis of quasi static experiments. The suitability of the speckle pattern was verified evaluating the mean intensity gradient (MIG), a widely used evaluation parameter based on the intensity variation characteristics of the speckle, defined in [25]. The obtained MIG values were between 35 and 37, ensuring a mean bias error of displacement of under 1% [25,26].

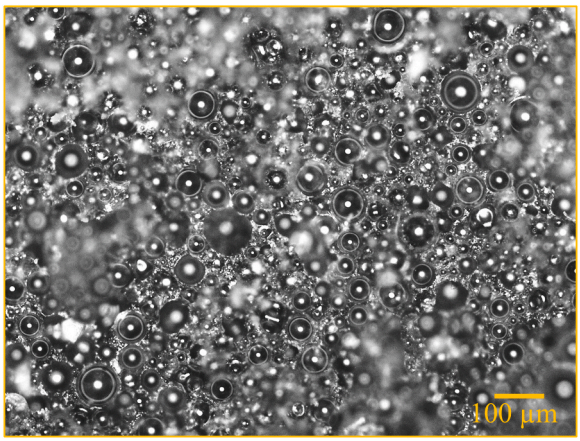

Fig. 2. Optical micrograph of the syntactic foam.

2.2. Test methods

2.2.1. Quasi-static tests

The quasi-static experiments were filmed by a high-resolution camera (JAI BM-500GE monochrome progressive scan camera) to measure deformation. The specimens were loaded by a screw-driven testing machine (Zwick Z250) via compression fixtures. A lubricant was used to minimize the effects of friction between the anvils and the sample. The uniaxial compression experiments were conducted under displacement control at a nominal strain rate of 10^{-3} s^{-1} in all experiments. The compressive force was measured by a 20 kN load cell. The strain histories were analysed using the GOM Aramis DIC software [27].

The temperature was varied from 0°C to 100°C. These temperatures were chosen based on the typical service and glass transition (54 °C) temperatures of the selected syntactic foam. The ambient temperature was regulated using a feedback-controlled environmental chamber, while lower than ambient temperatures were achieved by connecting a liquid nitrogen dewar to the inlet of the chamber. The flow rate of the liquid nitrogen was controlled automatically, and the temperature was monitored using a built-in thermocouple and an additional type-K thermocouple placed near the specimen. Once the target temperature was reached the sample was left in the chamber for an additional 20 minutes to reach temperature equilibrium prior to testing.

2.2.2. Dynamic tests

The high-rate response of the foam was measured using a Split Hopkinson Pressure Bar apparatus (SHPB) [28] which can produce stress pulses longer than 1 ms and therefore large compressive strains. The incident and transmitted bars, each with circular cross-section, had a diameter of 16 mm and were made of Ti64. The striker, input bar and output bar, were all 2.7 m in length and were supported by low-friction bearings. The stress waves in the bar were analysed as in [29] to construct the time history of strain and strain rate in the specimen and of the forces at the specimen's ends. A 1 mm thick cardboard disk (436 g/m^2) was used as a pulse shaper between the striker and the input bar. A schematic of the setup, similar to that in [18–30], is shown in

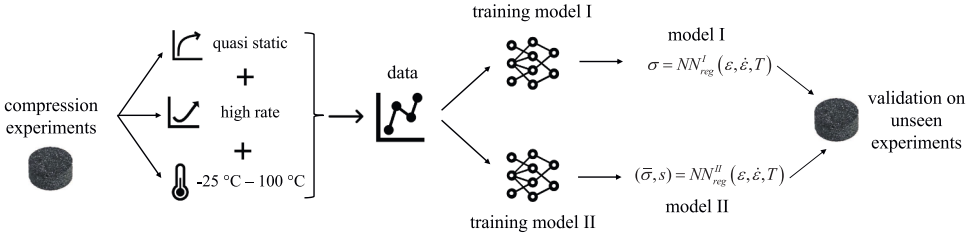

Fig. 1. Flowchart of the research process utilised in this study.

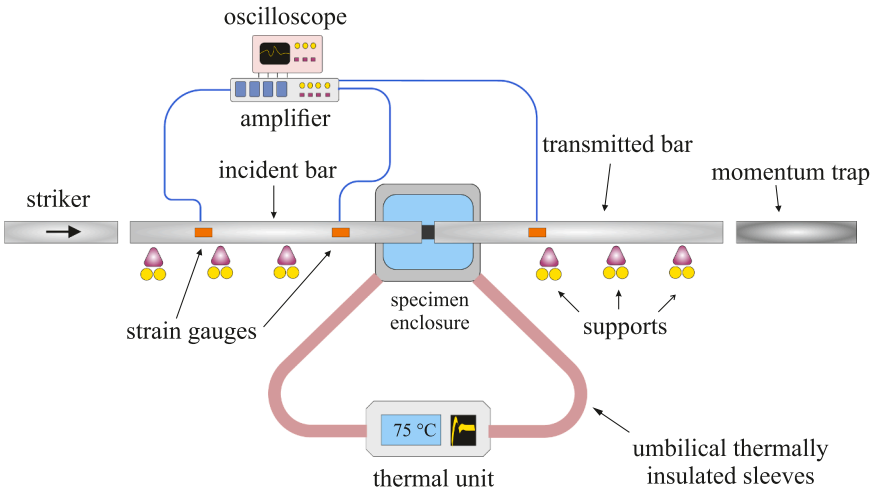

Fig. 3. Schematic of the Split Hopkinson pressure bar apparatus.

Fig. 3.

The temperature dependence of the high-rate response was examined across a temperature range of −25℃ to 100℃. The specimen temperature was regulated using a bespoke feedback-controlled environmental chamber (schematic in Fig. 3) following a procedure analogous to that employed during the quasi-static experiments. The projectile speed was adjusted to have strain rates varying in a narrow range, specifically [2200,2700] /s. The employed environmental chamber comprises a thermal unit, in which air is conditioned to higher or lower than ambient temperatures, a temperature controller, a specimen enclosure and two thermally insulated umbilical sleeves connecting the specimen enclosure to the air conditioning unit. The heated or refrigerated air is transferred to the enclosure by means of a suitable fan, embedded in the thermal unit. The temperature in the enclosure is fed back to the temperature controller by means of a type K thermocouple positioned inside the enclosure, in proximity to the sample.

The specimen enclosure is installed on the SHPB apparatus by enabling the incident and transmitted bars to be partially inserted within the specimen enclosure using low friction, thermally insulated bar supports (Fig. 4).

3. Results and discussion

3.1. Experimental results

A total of twelve high-rate and nine quasi-static experiments were conducted over a temperature range of −25°C to 100°C, as given in Table 1, detailing the number of repetitions. Two experiments were conducted for each loading case except for the quasi-static experiments conducted at temperatures of −25°C and 75°C due to limited material availability.

Table 1
Number of tests performed for quasi-static and high-rate experiments.

	-25 °C	0 °C	25 °C	50 °C	75 °C	100 °C
Quasi-static	0	2	2	2	1	2
High-rate	2	2	2	2	2	2

The influence of temperature on the quasi-static and high-rate compressive behaviour of the material is depicted in Fig. 5(a) and (b), respectively. The experiments show the typical response of a polymer foam with a prominent dependence of the compressive response on temperature and strain rate, with the stiffness and flow stress reducing with increasing temperature at both low and high strain rates. Fig. 5(c) illustrates the mechanical responses measured at room temperature, to highlight the strain rate sensitivity of the material, with the dynamic plateau stress more than double of its static counterpart.

Fig. 5(d) shows the detail of the data measured in a typical dynamic test at room temperature. The plot illustrates the incident (F_{inp}) and transmitted (F_{out}) force histories at the interfaces between the sample and the bars, as well as the evolution of the strain rate during the experiment. During dynamic experiments, a significant mismatch between the two forces indicates a non-uniform deformation along the sample. On the contrary, when the two forces are approximately equal it can be assumed that strains along the sample are uniform and, therefore, that the measured stress-strain characteristic is representative of the behaviour of the studied material [24]. It is clear that the specimen's incident and transmitted forces equalise in the early stages of the deformation, giving valid measurements of the stress history. After equilibrium and prior to densification the strain rate was approximately constant.

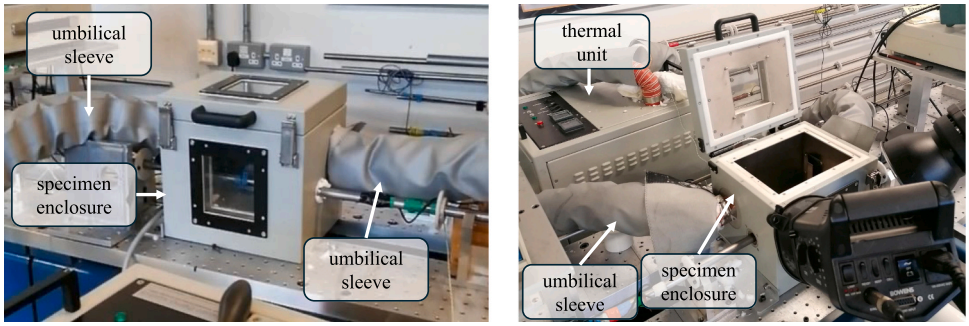

Fig. 4. Details of the experimental apparatus used for the high strain rate experiments.

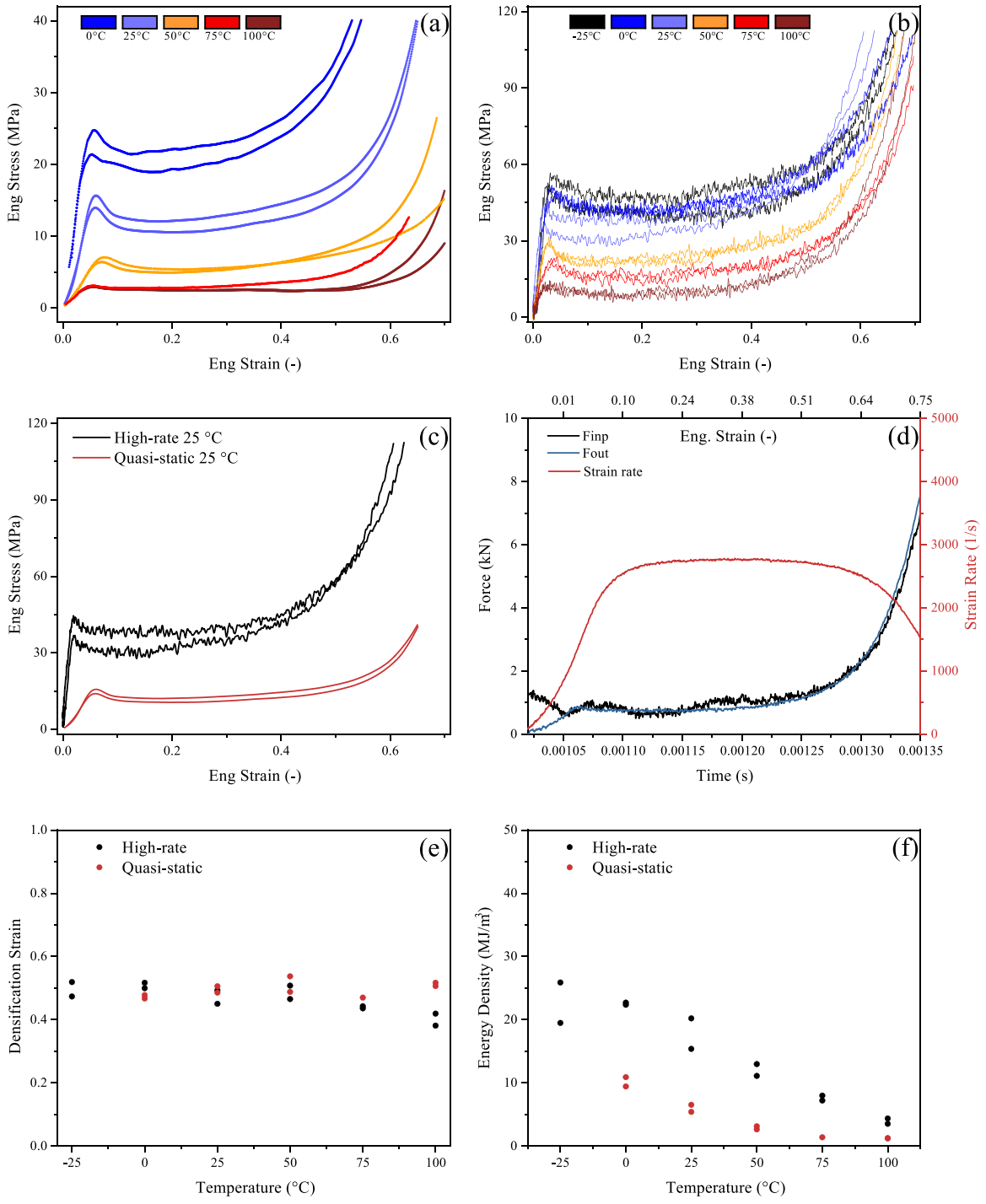

Fig. 5. Summary of the experimental results; (a) temperature dependence of the quasi-static response; (b) temperature dependence of the high-rate response; (c) rate dependence at room temperature; (d) force equilibrium and strain rate history; (e) sensitivity of the densification strain to temperature and strain rate; (f) sensitivity of the absorbed energy density to temperature and strain rate.

Fig. 5(e) and (f) analyse and compare the densification strain and the absorbed energy density at densification measured at different temperatures and strain rates. The absorbed energy density in Fig. 5(f) is calculated as the integral of each of the measured stress-strain curves in the strain interval included between zero and the densification strain [18]. Syntactic foams are typically used in protective structures for their capacity to dissipate significant mechanical energy while limiting the transmitted force. The densification strain is therefore chosen as the upper bound in the determination of the energy absorption, as beyond this limit stresses increase rapidly with the increase of strain.

The experimental findings suggest that the densification strain does not exhibit any noticeable dependence on temperature or strain rate. In contrast, the absorbed energy density displays a clear dependence on both temperature and strain rate. The experimental results indicate that the absorbed energy density in high-rate experiments is nearly twice that of quasi-static experiments, and it exhibits a decreasing trend with increasing temperature for both high-rate and quasi-static loading.

3.2. Implementation of the data-driven models

3.2.1. Training data sets

Data from eight quasi-static and eight high-rate experiments were used to assemble training datasets for two surrogate models. These experiments were repeated at low and high strain rates (10^{-3} /s and approximately 2500 /s, respectively) and at temperatures of 0°C, 25°C, 50°C, and 100°C; two repetitions were performed for each temperature and strain rate pair. The data from the remaining five experiments (carried out at −25°C and 75°C, Table 1) was stored to perform a validation of the predictions of the surrogate model.

Two surrogate models were developed: model I provides stress as a function of temperature, strain, and strain rate; model II provides both *average* stress and the *range of variation* of the stress as a function of the same inputs. Fig. 6 illustrates the training datasets I and II, used to train model I and II, respectively. Quasi-static and high-rate experiments are shown separately for clarity of visualisation, but they were used together in the training process.

Training dataset I in Fig. 6(a) and (c) was assembled from the stress-strain histories after smoothing (using the adjacent-averaging signal processing method with the point of window 20). It comprised 13600 data points, with a similar amount of data points for each experiment.

Training dataset II was assembled as a stochastic dataset to carry information on the uncertainty of the stress versus strain histories. The raw (unfiltered) stress/strain data was divided into strain intervals (bins) of width 0.01. For each bin, the mean of strain and the mean and range of stress were calculated, considering data from both repetitions of the experiments. The stochastic dataset was assembled to have as entries mean strain, mean stress and stress range in each of the strain intervals; it is shown in Fig. 6(b) and (d), with the error bars representing the stress range. The dataset comprised a total of 521 data points, with a similar amount of data points (60−70) for each experiment.

3.2.2. Surrogate models

Feed forward neural networks (NNs) [31] were used to construct the surrogate models. Two different models are presented, and their architecture is summarised in Fig. 7. Model I receives as inputs the compressive strain, temperature and strain rate, providing the value of the compressive stress, $\sigma = NN^{I}_{reg}(\varepsilon, \dot{\varepsilon}, T)$. The inputs for Model II are again strain, temperature and strain rate, and the outputs are mean $\overline{\sigma}$ and range s of the stress, $(\overline{\sigma}, s) = NN^{II}_{reg}(\varepsilon, \dot{\varepsilon}, T)$. The architecture of both neural networks was determined through iterative experimentation; the networks comprised 2 hidden layers with 100 and 64 neurons.

A more explicit mathematical representation of the two models is given below [31].

$$\sigma = w^{I[3]}_{ij} f^{I[2]}_{i}\left(w^{I[2]}_{jk} f^{I[1]}_{k}\left(w^{I[1]}_{kl} x_l + b^{I[1]}_{k}\right) + b^{I[2]}_{j}\right) + b^{I[3]}_{i} \tag{1}$$

$$(\overline{\sigma}, s) = w^{II[3]}_{ij} f^{II[2]}_{i}\left(w^{II[2]}_{jk} f^{II[1]}_{k}\left(w^{II[1]}_{kl} x_l + b^{II[1]}_{k}\right) + b^{II[2]}_{j}\right) + b^{II[3]}_{i} \tag{2}$$

Where:

- x_l is the input vector, i.e. $(\varepsilon, \dot{\varepsilon}, T)$
- $w^{I[n]}$ and $w^{II[n]}$ are the weight matrices of each layer 'n' for the first and for the second model, respectively. The weights determine the influence of the input on the output of each neuron; their value is optimised during the training process.
- $b^{I[n]}$ and $b^{II[n]}$ are the bias vectors of each layer 'n', for the first and for the second model. The biases are adjusted during the training process and introduce a certain level of tendency towards specific outcomes or behaviours.

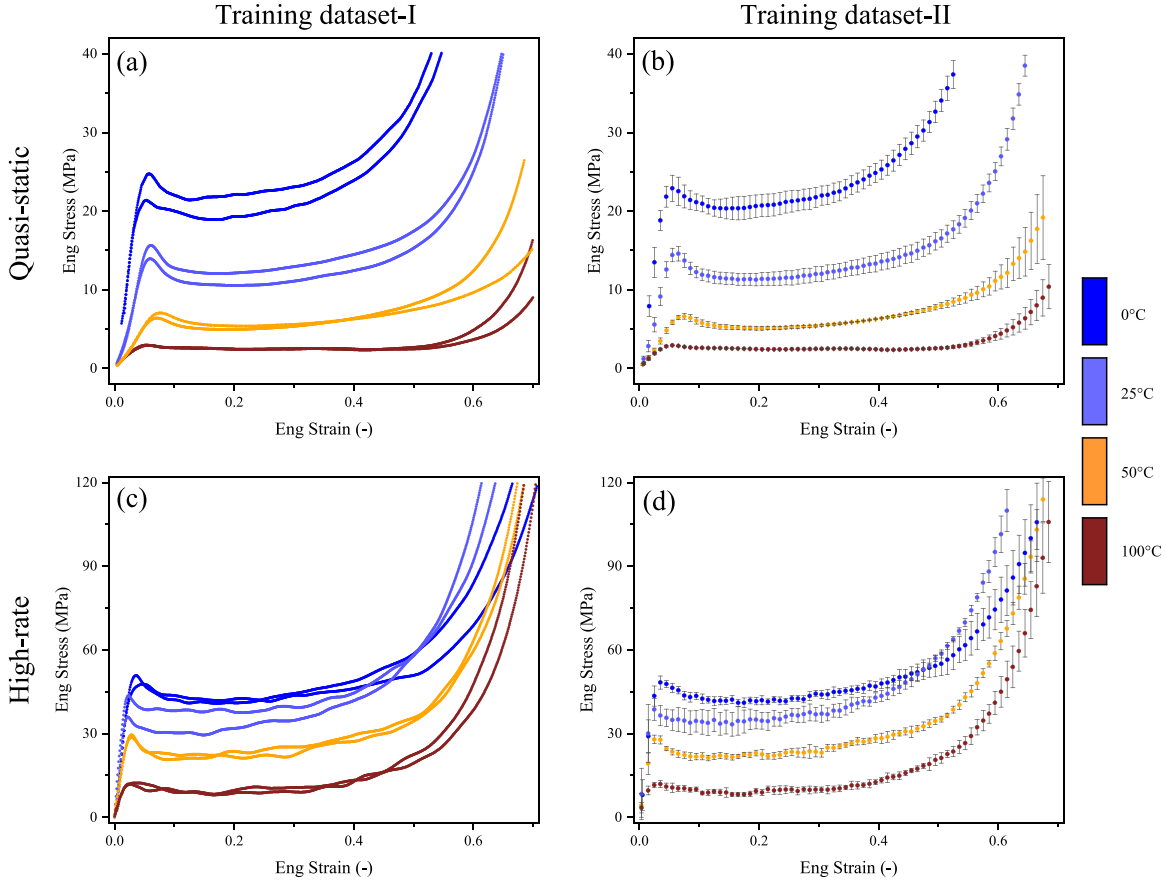

Fig. 6. Experimental datasets utilised by the two data-driven models.

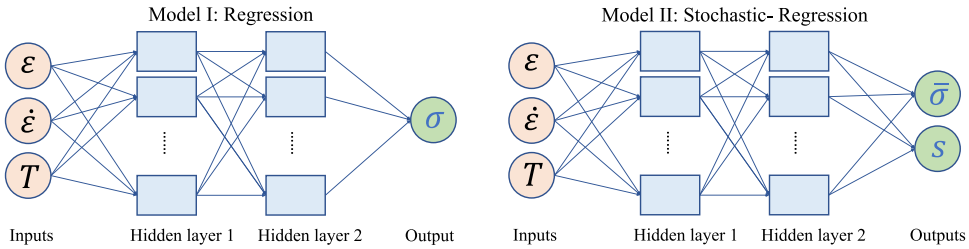

Fig. 7. Schematic of the two surrogate models.

- $f^{I[n]}$ and $f^{II[n]}$ are the activation functions [31] of each layer 'n', for the first and for the second model.
- The integer 'n' indicates the layer, where n=1 and n=2 represent the two hidden layers, and n=3 refers to the output layer.

The inputs and outputs values were rescaled to a range between 0 and 1 using the Minmax() function [32]; the ReLU [33] function was selected as the activation function for the hidden layers, while the identity function was applied to the output layer (i.e. no activation). The selected loss function was the mean square error (MSE) [32]. The NN was trained in TensorFlow 2.6 [34] via backpropagation, employing the Adam optimiser [35] with a learning rate of 0.001. Model I was trained for 1000 epochs with a batch size of 400, whereas Model II was trained for 2500 epochs with a batch size of 26. The training datasets I and II were split into 90% and 10% subsets used for training and testing, respectively.

3.2.3. *Assessment of the accuracy of the surrogate model*

To test the fidelity of the surrogate models, the data recorded in 5 experiments (two high-rate conducted at $-25°C$, two high-rate at $75°C$, and one quasi-static at $75°C$), unseen by the training process, was used as a benchmark for the models' predictions. It is worth emphasising that

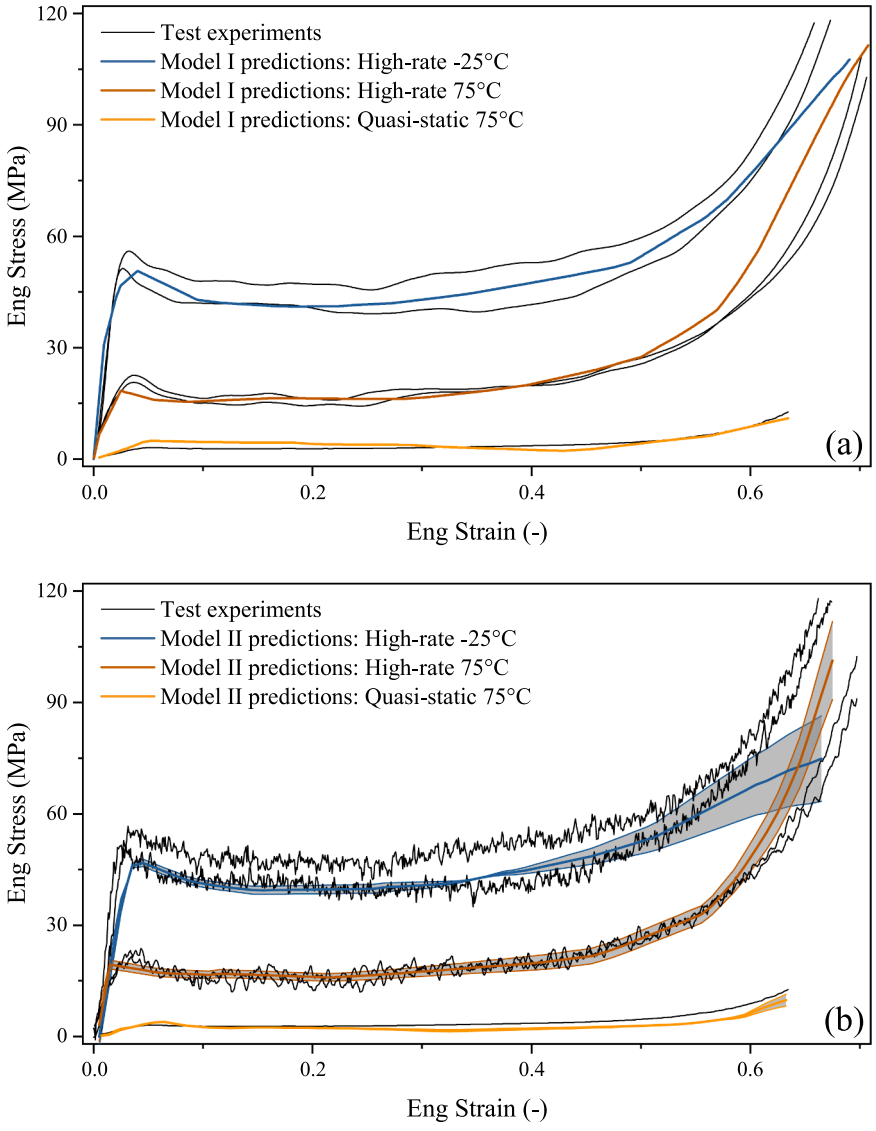

Fig. 8. Predictions of the stress/strain responses in experiments not included in the training dataset, by (a) Model I and (b) Model II.

assessing the models on unseen data provides a more accurate evaluation of their performance in real prediction scenarios. On the contrary, evaluating the models on data used during the training process generally yields optimistic performance metrics that may not represent how the models would perform when predicting new, unseen data.

Data from the 5 unseen tests mentioned above was processed as described in 3.1 above. The surrogate models were used to predict the stress versus strain responses corresponding to these five experiments. Starting from the initial configuration $\varepsilon = \sigma = 0$, the strain was progressively increased and the models used to compute σ, $\overline{\sigma}$ and s.

3.3. Discussion

Fig. 8 presents the predictions of the models for the 5 unseen tests. The surrogate models are found to be in good agreement with the experiments, accurately predicting the temperature and strain-rate dependent stress/strain responses of the material until densification. The models therefore show good generalisation capabilities, as demonstrated by their ability to perform well on unseen data; it is particularly noteworthy that accurate predictions are achieved by both models even for tests at −25°C, despite data at this temperature is not only unseen during the training, but also outside the range of the training dataset, and therefore the models are extrapolating.

The densification strain of the foam as the strain at maximum energy absorption is calculated according to Eq. (3) [36,37].

$$\eta = \frac{1}{\sigma(\varepsilon)} \int_0^{\varepsilon} \sigma(\varepsilon) d\varepsilon. \tag{3}$$

This efficiency is plotted in Fig. 9(a) to illustrate the definition. Fig. 9 (b) and (c) compare the predictions of densification strain and energy density (at densification) provided by the surrogate models with the ground truth represented by the experimental data. Both models give good predictions of both densification strain and energy density at densification. It is worth noting that the experimental data in Fig. 9(b) and (c) were not included in the neural networks training process.

Fig. 8(b) showed that model II gives the highest errors in the elasticity-dominated early stages of deformation ($0 \leq \varepsilon \leq 0.1$) and in the densification regime ($\varepsilon \geq 0.5$). This is likely because these deformation phases occupy narrow portions of the input space. To address this issue, binning of the data with a width of 0.01, as applied to the rest of the stress-strain curves, is not utilized in these regions. Instead, the bin size is progressively reduced to 0.001, as depicted in Fig. 10. The figure also demonstrates the enhanced predictions of the stress/strain curve for the previously unseen high-rate experiment conducted at 75 °C.

To demonstrate the capability of the model, the stress/strain curve is predicted under the imposition of a temperature history during deformation. It is assumed that the temperature T varies according to $T = T_0 + \alpha\varepsilon$, where $T_0 = 25°C$, $\alpha$is a parameter and $\varepsilon$is the compressive strain. Fig. 11 shows the stress versus strain predictions of model I for 3 selected values of α, representing a constant temperature of $T_0 = 25°C$, a temperature increasing from $T_0 = 25°C$ to 100°C at $\varepsilon = 0.6$, and a

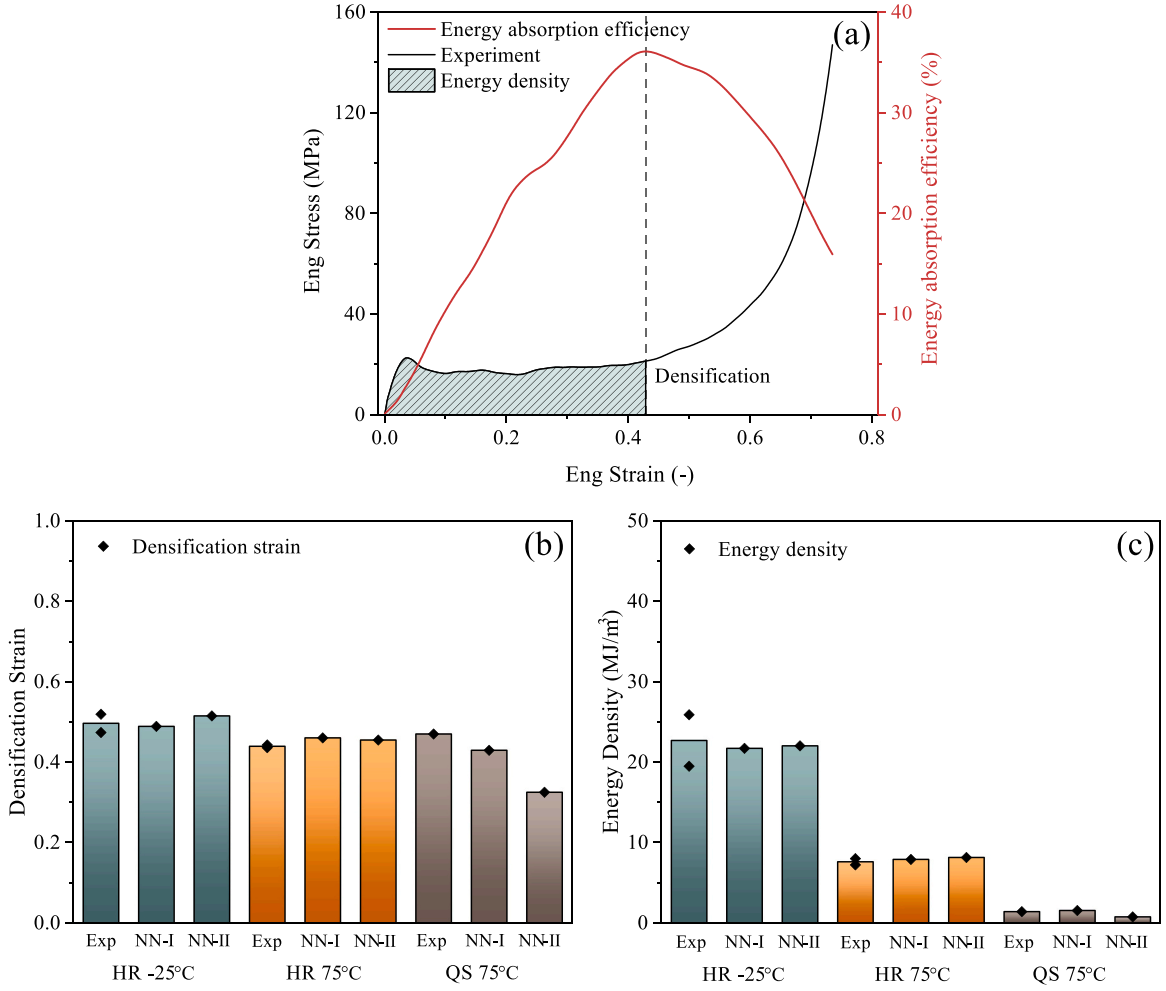

Fig. 9. (a) Definition of densification strain and energy absorption efficiency illustrated on a high-rate experiment conducted at 75°C; (b), (c) comparisons between the predictions of the surrogate models and unseen experimental data.

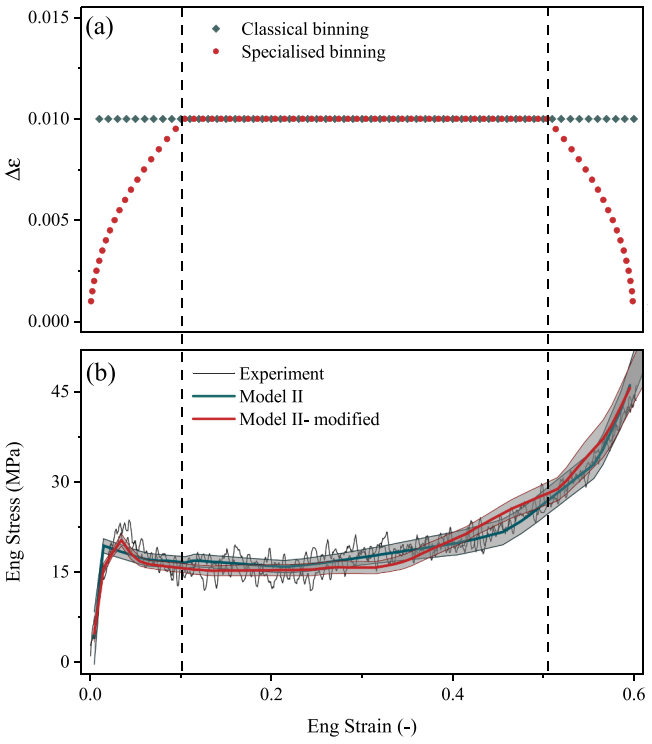

Fig. 10. The effect of the non-uniform binning of the data in the training database II on the predictive accuracy of the high-rate experiment conducted at 75 °C.

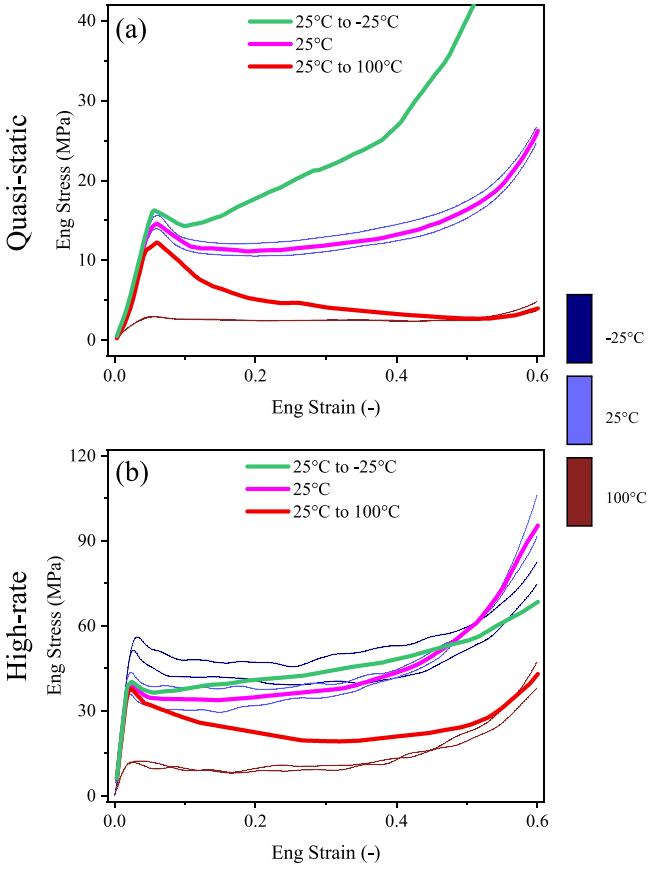

Fig. 11. Examples of the predictive capabilities of model I.

temperature decreasing from $T_0 = 25°C$ to $-25°C$ at $\varepsilon = 0.6$. The predictions are shown together with measurements at constant T and show the expected trends.

4. Conclusions

The stress-strain histories recorded in quasi-static and high-rate compression experiments on a syntactic foam at different temperatures were used to assemble a training dataset to develop data-driven surrogate models able to predict the stress history of a syntactic foam, and its variability, as a function of the imposed strain, temperature and strain rate. The surrogate models were tested on unseen experiments demonstrating high accuracy, and successful predictions even when extrapolating. A technique to manipulate the training database in order to improve the quality of the regression is also proposed and its effectiveness is demonstrated. The proposed data-driven surrogate models are informed exclusively by a relatively limited number of experiments. This approach eliminates the potential limitations of traditional phenomenological constitutive equations by learning directly from experimental data. Both models can capture the non-linear phase following the collapse stress without the need to calibrate complex constitutive equations. An additional advantage lies on the ability of the second surrogate model to preserve the information contained in the variability of the experimental data.

CRediT authorship contribution statement

Burcu Tasdemir: Writing – original draft, Visualization, Methodology, Investigation, Formal analysis. **Vito L. Tagarielli:** Writing – review & editing, Validation, Supervision, Methodology, Conceptualization. **Antonio Pellegrino:** Writing – review & editing, Supervision, Investigation, Funding acquisition, Conceptualization.

Declaration of Competing Interest

The authors declare that they have no known competing financial interests or personal relationships that could have appeared to influence the work reported in this paper.

Data availability

Data will be made available on request.

References

[1] N. Gupta, S.E. Zeltmann, V.C. Shunmugasamy, D. Pinisetty, Applications of polymer matrix syntactic foams, JOM 66 (2014) 245–254.
[2] N. Gupta, V.C. Shunmugasamy, High strain rate compressive response of syntactic foams: Trends in mechanical properties and failure mechanisms, Mater. Sci. Eng.: A 528 (2011) 7596–7605.
[3] B. Song, W. Chen, D.J. Frew, Dynamic Compressive Response and Failure Behavior of an Epoxy Syntactic Foam, J. Compos. Mater. 38 (2004) 915–936.
[4] A. Pellegrino, V.L. Tagarielli, R. Gerlach, N. Petrinic, The mechanical response of a syntactic polyurethane foam at low and high rates of strain, Int. J. Impact Eng. 75 (2015) 214–221.
[5] B. Song, W.W. Chen, W.-Y. Lu, Mechanical characterization at intermediate strain rates for rate effects on an epoxy syntactic foam, Int. J. Mech. Sci. 49 (2007) 1336–1343.
[6] V.C. Shunmugasamy, N. Gupta, N.Q. Nguyen, P.G. Coelho, Strain rate dependence of damage evolution in syntactic foams, Mater. Sci. Eng.: A 527 (2010) 6166–6177.
[7] B.R. Bharath Kumar, A.K. Singh, M. Doddamani, D.D. Luong, N. Gupta, Quasi-Static and High Strain Rate Compressive Response of Injection-Molded Cenosphere/HDPE Syntactic Foam, JOM 68 (2016) 1861–1871.
[8] Z. Fan, Y. Miao, Z. Wang, B. Zhang, H. Ma, Effect of the cenospheres size and internally lateral constraints on dynamic compressive behavior of fly ash cenospheres polyurethane syntactic foams, Compos. Part B 171 (2019) 329–338.
[9] P. Jakkula, G.C. Ganzenmüller, S. Beisel, P. Rüthnick, S. Hiermaier, The Symmpact: A Direct-Impact Hopkinson Bar Setup Suitable for Investigating Dynamic Equilibrium in Low-Impedance Materials, Exp. Mech. 62 (2022) 213–222.
[10] D. Janoff, Flexible, High Temperature Thermal Insulation Materials for Subsea Wellhead and Production Equipment, ASME 2002 21st Int. Conf. Offshore Mech. Arct. Eng. (2009) 291–299.

[11] W.-T. Wang, L. Watkins, Syntactic Foam Thermal Insulation for Ultradeep High Temperature Applications, ASME 2002 21st Int. Conf. Offshore Mech. Arct. Eng. (2009) 155–166.
[12] E. Linul, D. Lell, N. Movahedi, C. Codrean, T. Fiedler, Compressive properties of zinc syntactic foams at elevated temperatures, Compos. Part B: Eng. 167 (2019) 122–134.
[13] K. Myers, B. Katona, P. Cortes, I.N. Orbulov, Quasi-static and high strain rate response of aluminum matrix syntactic foams under compression, Compos. Part A: Appl. Sci. Manuf. 79 (2015) 82–91.
[14] N. Movahedi, T. Fiedler, A. Tasdemirci, G.E. Murch, I.V. Belova, M. Güden, Impact loading of functionally graded metal syntactic foams, Mater. Sci. Eng.: A 839 (2022) 142831.
[15] L.J. Gibson, Cellular Solids, MRS Bull. 28 (2003) 270–274.
[16] B. Song, W. Chen, T. Yanagita, D.J. Frew, Temperature effects on dynamic compressive behavior of an epoxy syntactic foam, Compos. Struct. 67 (3) (2005) 289–298.
[17] C.S. Tan, J.A. Rongong, E. Ghassemieh, Temperature and strain rate dependence of syntactic foam under tensile and shear loads, Proc. Inst. Mech. Eng., Part L: J. Mater.: Des. Appl. 227 (1) (2013) 26–37.
[18] Y. Chen, G. Quino, A. Pellegrino, A comprehensive investigation on the temperature and strain rate dependent mechanical response of three polymeric syntactic foams for thermoforming and energy absorption applications, Polym. Test. 130 (2024) 108287.
[19] B. Tasdemir, A. Pellegrino, V. Tagarielli, A strategy to formulate data-driven constitutive models from random multiaxial experiments, Sci. Rep. 12 (2022) 22248, https://doi.org/10.1038/s41598-022-26051-y.
[20] B. Tasdemir, V. Tagarielli, A. Pellegrino, A data-driven model of the yield and strain hardening response of commercially pure titanium in uniaxial stress, Mater. Des. 229 (2023) 111878.
[21] K. Yanamandra, G.L. Chen, X. Xu, G. Mac, N. Gupta, Reverse engineering of additive manufactured composite part by toolpath reconstruction using imaging and machine learning, Compos. Sci. Technol. 198 (2020) 108318.
[22] P. Siegkas, Generating 3D porous structures using machine learning and additive manufacturing, Mater. Des. 220 (2022) 110858.
[23] C.-T. Chen, G.X. Gu, Machine learning for composite materials, MRS Commun. 9 (2019) 556–566.
[24] G.T. Gray III, Classic split-Hopkinson pressure bar testing, ASM Handb., Mech. Test. Eval. 8 (2000) 462–476.
[25] B. Pan, Z. Lu, H. Xie, Mean intensity gradient: An effective global parameter for quality assessment of the speckle patterns used in digital image correlation, Opt. Lasers Eng. 48 (2010) 469–477.
[26] G. Quino, Y. Chen, K.R. Ramakrishnan, F. Martínez-Hergueta, G. Zumpano, A. Pellegrino, N. Petrinic, Speckle patterns for DIC in challenging scenarios: rapid application and impact endurance, Meas. Sci. Technol. 32 (2020) 015203.
[27] M. Gom, ARAMIS v6. 1 User Manual-Software, (2009).
[28] H. Kolsky, An Investigation of the Mechanical Properties of Materials at very High Rates of Loading, Proc. Phys. Soc. B. 62 (1949) 676.
[29] F. De Cola, A. Pellegrino, C. Glößner, D. Penumadu, N. Petrinic, Effect of Particle Morphology, Compaction, and Confinement on the High Strain Rate Behavior of Sand, Exp. Mech. 58 (2018) 223–242.
[30] A. Pellegrino, M.J. Perez-Martin, K. Dragnevski, G. Zumpano, N. Petrinic, Temperature and strain rate dependent mechanical response of METCO 601 aluminium-polyester abradable seal coating, EPJ Web Conf. 183 (2018) 04012.
[31] I. Goodfellow, Y. Bengio, A. Courville, Deep Learning, MIT Press, 2016.
[32] F. Pedregosa, G. Varoquaux, A. Gramfort, V. Michel, B. Thirion, O. Grisel, M. Blondel, A. Müller, J. Nothman, G. Louppe, P. Prettenhofer, R. Weiss, V. Dubourg, J. Vanderplas, A. Passos, D. Cournapeau, M. Brucher, M. Perrot, É. Duchesnay, Scikit-learn: Machine Learning in Python, arXiv [cs.LG]. (2012) 2825–2830. https://www.jmlr.org/papers/volume12/pedregosa11a/pedregosa11a.pdf?ref=https:/ (accessed January 30, 2024).
[33] C. Nwankpa, W. Ijomah, A. Gachagan, S. Marshall, Activation Functions: Comparison of trends in Practice and Research for Deep Learning, arXiv [cs.LG]. (2018). http://arxiv.org/abs/1811.03378.
[34] P. Singh, A. Manure, Introduction to TensorFlow 2.0. Learn TensorFlow 2.0, Apress, Berkeley, CA, 2020, pp. 1–24.
[35] D.P. Kingma, J.A. Ba, A Method for Stochastic Optimization in 3rd International Conference on Learning Representations, ICLR 2015, San Diego, CA, USA, May 7-9, 2015, Conference Track Proceedings (eds Bengio, Y. & LeCun, Y.)(2015).
[36] E.A. Flores-Johnson, Q.M. Li, Indentation into polymeric foams, Int. J. Solids Struct. 47 (2010) 1987–1995.
[37] Q.M. Li, I. Magkiriadis, J.J. Harrigan, Compressive strain at the onset of densification of cellular solids, J. Cell. Plast. 42 (2006) 371–392.